

The 6.7-GHz and 25-GHz methanol masers in OMC-1

M. A. Voronkov^{1,2*}, A. M. Sobolev³, S.P. Ellingsen⁴, A.B.Ostrovskii⁵

¹Australia Telescope National Facility CSIRO, Locked Bag 194, Narrabri, NSW 2390, Australia

²Astro Space Centre, Profsouznaya st. 84/32, 117997 Moscow, Russia

³Astronomical Observatory of the Ural State University, Lenin pr-t. 51, 620083 Ekaterinburg, Russia

⁴School of Mathematics and Physics, University of Tasmania, GPO Box 252-37, Hobart, Tasmania 7000, Australia

⁵Ural State University, Lenin pr-t. 51, 620083 Ekaterinburg, Russia

ABSTRACT

The Australia Telescope Compact Array (ATCA) has been used to search for methanol maser emission at 6.7 GHz towards OMC-1. Two features peaking at 7.2 km s^{-1} and -1.1 km s^{-1} have been detected. The former has at least two components close in both velocity and position. It is located south-east of the Orion Kleinmann-Low (Orion-KL) nebula in the region of outflow traced by the 25-GHz methanol masers and the 95-GHz methanol emission. It is shown by modelling that in contrast to the widespread opinion that simultaneous masing of methanol transitions of different classes is impossible there are conditions for which simultaneous masing of the class II transition at 6.7-GHz and some class I transitions (e.g. the series at 25 GHz) is possible. A relevant example is provided, in which the pumping occurs via the first torsionally excited state and is driven by radiation of the dust intermixed with the gas in the cloud. In this regime the dust temperature is significantly lower ($T \approx 60 \text{ K}$) than in the case of bright 6.7-GHz masers ($T > 150 \text{ K}$). The narrow spectral feature at -1.1 km s^{-1} has a brightness temperature greater than about 1400 K, which suggests that it is probably a maser. It emanates from the Orion South region and is probably associated with the approaching part of outflow seen in CO. The 25-GHz maser associated with OMC-1 was observed quasi-simultaneously with the 6.7-GHz observations. No 25-GHz emission associated with the -1.1 km s^{-1} 6.7 GHz feature towards Orion South was detected.

Key words: masers – ISM: molecules – ISM: individual objects: OMC-1

1 INTRODUCTION

The Orion Molecular Cloud 1 (OMC-1) is a well known region of massive star formation containing several young stellar objects (YSOs) at the very early stages of their formation as well as outflows related to them (see, e.g. the review by Genzel & Stutzki 1989). Methanol masers in a variety of transitions are often found in such regions. Masing transitions are traditionally divided into two classes. Although masers of both classes often co-exist in the same star-forming region, they are usually seen apart from each other (Menten 1991a,b).

OMC-1 harbours strong class I methanol masers. These masers are believed to trace distant parts of the outflows from YSOs and are associated with the early stages of the massive star formation (e.g., Menten 1991a; Ellingsen 2005). The strongest (about 150 Jy) masers of the J_2-J_1 E line series near 25 GHz are observed in OMC-1 and have inspired numerous observational and theoretical studies (see, e.g., Menten et al. 1988c; Johnston et al. 1992; Sobolev, Watson & Okorokov 2003).

In contrast, strong class II masers have not been detected in OMC-1. Only weak emission in the strongest class II $5_1 - 6_0 A^+$ transition at 6.7 GHz has been reported from this source by Caswell et al. (1995), and it was unclear whether the observed spectral line is a maser or has a quasi-thermal origin (i.e., the level populations are without inversion). Currently, class II methanol masers are thought to appear in the vicinity of the massive young stellar objects (YSOs) at the early stages of ultra-compact HII region (UCHII) evolution (e.g., Ellingsen et al. 1996; Minier et al. 2001; Codella et al. 2004). The transition at 6.7 GHz manifests flux densities which are the highest among methanol masers and can reach 5000 Jy. Maser emission from this transition is widespread and to date has been detected towards more than 500 sources (see, e.g. the compilation by Malyshev & Sobolev 2003). Being the strongest this transition is the best prospect for searches for new class II methanol maser sites.

Evolutionary stages of the massive YSOs at which different classes of methanol masers exist do intersect considerably. Ellingsen (2005) detected class I methanol masers at 95.1 GHz towards 38% of a statistically complete sample of the class II masers at 6.7 GHz. No extensive search of class II masers has been per-

* E-mail: Maxim.Voronkov@csiro.au

Table 1. Dates of observations and a summary of array configurations. The compact H75B configuration featured the north-south spur of the ATCA providing a better uv-coverage for equatorial sources. In the 1.5D configuration session the CA05 antenna did not observe and, therefore, the second shortest baseline CA04–CA05 was not available. Other sessions had all 6 antennae working.

Date UT	Array configuration	Baseline length (m)		
		Min	Max no CA06	Max with CA06
9–10 June 2003	H75B	31	89	4408
12 November 2003	1.5D	107	1439	4439
5 January 2004	6A	337	2923	5939
10 April 2004	EW367	46	367	4408

formed towards the positions of isolated class I masers. This is partly due to the lack of information about such sources since most class I masers have been found towards known class II masers, which are often located within a single dish beam (e.g., Slysh et al. 1994).

Therefore, among known sources OMC-1 is somewhat exceptional: it possesses strong class I masers produced by an outflow (Johnston et al. 1992), while there are no strong class II masers associated with the YSO producing this outflow. Recent observations have shown that some hydroxyl masers and class II methanol masers can also be associated with outflows (Argon, Reid & Menten 2003; Codella et al. 2004). This is supported by statistical analysis of correlation between the maser velocities and those of the molecular outflow tracers (Malyshev & Sobolev 2003) and is reasonable because the methanol abundance is significantly increased in the interface regions, where the outflow interacts with the ambient material (e.g., Bachiller et al. 1995, 1998; Gibb & Davis 1998). It is presently unclear whether weak class II masers can co-exist with the class I masers or they always trace different parts of outflow. We have undertaken a sensitive search at 6.7 GHz in order to figure out whether there are weak class II masers in the vicinity of the YSOs and outflows in OMC-1. The 25-GHz class I maser in OMC-1 was reobserved to check its current status.

2 OBSERVATIONS

The observations were made using the Australia Telescope Compact Array (ATCA). Details on the array configurations¹ and observing dates are summarized in Table 1. During the first session on 2003 June 9–10, the 25-GHz maser was observed quasi-simultaneously with the 6.7-GHz observations in 7 short scans switching the frequency approximately every 90 minutes. The primary aim of the subsequent sessions was to estimate the 6.7-GHz source size and therefore the 25-GHz transition was not observed. The adopted rest frequencies are 24959.080 MHz and 6668.5192 MHz for $5_2 - 5_1$ E and $5_1 - 6_0$ A⁺ methanol transitions respectively (Lovas 1992; Breckenridge & Kukulich 1995). For both frequencies and all sessions the correlator was configured to split the 4-MHz bandwidth into 1024 spectral channels yielding a spectral resolution of 3.9 kHz or 0.05 km s⁻¹ at 25 GHz

¹ More details on the ATCA configurations and baseline length distribution are available on the web http://www.narrabri.atnf.csiro.au/operations/array_configurations/configurations.html

and 0.18 km s⁻¹ at 6.7 GHz (no Hanning smoothing has been applied). Two orthogonal linear polarizations were observed at each frequency, except the CA01 antenna in the first session on 2003 June 9–10 which observed only horizontal polarization (at both frequencies) due to technical problems. During the data reduction the source has been assumed to be unpolarized and both polarizations, if presented, were averaged together. The position of the phase and pointing centre was $\alpha_{2000} = 5^h 35^m 15^s.069$, $\delta_{2000} = -5^\circ 23' 42''.53$ for the first session and $\alpha_{2000} = 5^h 35^m 15^s.439$, $\delta_{2000} = -5^\circ 23' 07''.0$ for the latter observations. The full width at half maximum (FWHM) of the primary beam was 7'.2 at 6.7 GHz and 2'.0 at 25 GHz. The global pointing solution was used for both frequencies giving an rms pointing accuracy of 5–10".

Most of the data reduction was performed using the MIRIAD package (13 May 2004 release) following standard procedures with the exception of bandpass calibration for the 6.7-GHz observations. We found that the accuracy of the bandpass calibration limited our ability to detect a weak spectral line. The shape of the uncalibrated bandpass was reasonably straight within the small part of the band occupied by the source spectrum and it was therefore safe to skip the bandpass calibration. However, this approach fails on the shortest baselines. The continuum emission is very strong towards OMC-1 at short spacings. Therefore, it is difficult to subtract this continuum accurately without a proper bandpass calibration, which would require unrealistically long observations of the bandpass calibrator. A residual error in the continuum subtraction tends to create weak and broad spurious lines in the spectrum. A similar problem makes it extremely difficult to observe a weak spectral line towards a strong continuum source using a single dish. Therefore, all the 6.7-GHz data resulting from baselines with a projected spacing shorter than 50m were flagged. This has a serious impact on the 6.7-GHz observations using the H75B array configuration, where about one half of the data was discarded. Shadowing was also a problem in the compact H75B array configuration throughout the whole session. All the 25-GHz data from baselines with a shadowed antenna have been flagged (3 per cent of visibilities from the total number of baselines without the CA06 antenna). The rejection of short spacings at 6.7 GHz discards all shadowed baselines automatically. During imaging, natural weighting was used to minimize the noise in the image and to provide better stability in the deconvolution algorithm (CLEAN) for the near-equatorial source. The data resulting from the long baselines with the CA06 antenna were used for non-imaging analysis only. In all sessions except the first one the standard ATCA primary calibrator 1934-638 was used for the amplitude calibration. For the first session 0605-085 with the adopted flux density of 1.8 Jy at 6.7 GHz was used instead due to the sidereal time range allocated. The 25-GHz data were corrected for the atmospheric opacity using archival meteorological data and the flux density scale was calibrated using observations of Uranus. The PLBOOT task of MIRIAD was used to compute the scale factor from the planetary observations using a built-in ephemeris. For the date of 25-GHz observations it implied the total flux density of Uranus equal to 0.76 Jy. The continuum source 0539-057 was used as a secondary calibrator at both frequencies. Although the calibration and imaging were performed in the MIRIAD, the AIPS++ package developed by NRAO² was used for a direct manipulation of the

² The National Radio Astronomy Observatory (NRAO) is a facility of the National Science Foundation operated under cooperative agreement by Associated Universities, Inc.

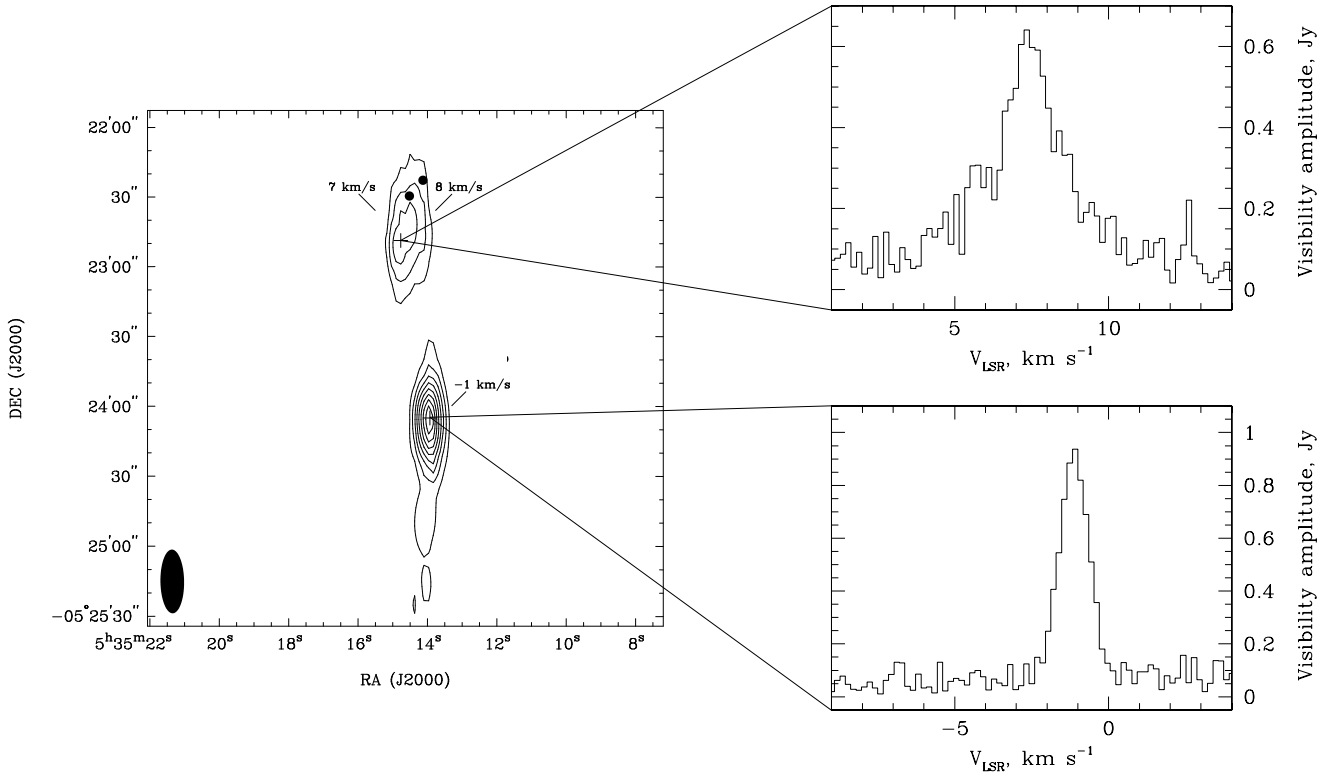


Figure 1. A cumulative image of the 6.7-GHz methanol emission in OMC-1 (all data except those resulted from the CA06 antenna have been used) and the spectra (a vector averaging of all data corresponding to uv-distances less than $5 \text{ k}\lambda$ has been used) at the peak positions for each feature. The filled ellipse represent the FWHM of the synthesized beam of $27.4'' \times 10.2''$ and its position angle of 0.8° . Contours are 20, 30, 40, 50, 60, 70, 80 and 90 per cent of $0.49 \text{ Jy beam}^{-1}$. The two filled circles represent Irc2 (lower) and BN (upper) objects.

Table 2. Results of the Gaussian fitting to 6.7-GHz images of individual spectral channels. All uncertainties are formal errors of the Gaussian fit. A good estimate of the actual 1σ positional accuracy is $5'' \times 2''$ (full width) with a positional angle of 0.8° (the synthesized beam has the FWHM of $27.4'' \times 10.2''$ and the same positional angle).

LSR Velocity (km s^{-1})	α_{2000} $5^{\text{h}}35^{\text{m}}$ ($^{\text{s}}$)	δ_{2000} -5° ($''$)	Peak flux (Jy)	Total flux (Jy)	Fitted Gaussian			Deconvolved Gaussian		
					maj ($''$)	min ($''$)	PA ($^\circ$)	maj ($''$)	min ($''$)	PA ($^\circ$)
-1.1	13.93 ± 0.02	$24'05''3 \pm 0.9$	0.45 ± 0.03	0.52	31 ± 3	10 ± 1	1 ± 3	unresolved		
7.2	14.77 ± 0.11	$22'49'' \pm 6$	0.20 ± 0.03	0.54	53 ± 20	14 ± 6	-7 ± 9	45 ± 23	9 ± 10	-9 ± 24
7.3	14.60 ± 0.05	$22'37'' \pm 2$	0.19 ± 0.02	0.48	44 ± 7	16 ± 3	-13 ± 6	35 ± 9	10 ± 5	-21 ± 19
7.5	14.53 ± 0.05	$22'42'' \pm 2$	0.22 ± 0.02	0.57	43 ± 8	17 ± 3	0 ± 6	33 ± 10	14 ± 4	-1 ± 21
7.9	14.37 ± 0.06	$22'46'' \pm 2$	0.17 ± 0.01	0.42	40 ± 8	17 ± 4	-5 ± 8	29 ± 11	13 ± 5	-10 ± 32

6.7-GHz data to investigate the behavior of the visibility amplitude at different uv-distances.

3 RESULTS

3.1 The 6.7-GHz data

To analyze the spatial and velocity distribution of the 6.7-GHz emission in OMC-1 we constructed a spectral cube and vector averaged spectra at different positions. All data from all sessions, except those including the CA06 antenna were used to produce the cube. A vector averaging (i.e. averaging of complex visibilities with phase) was used for the spectra because the signal was not strong enough for other methods of presentation. To avoid decorrelation in

the spectra only data corresponding to uv-distances less than $5 \text{ k}\lambda$ were included. A cumulative image of the source obtained from the cube is shown in Fig. 1 along with the spectra. The brightness of each pixel is the maximum across the velocity axis (different planes of the cube correspond to different spectral channels and, thus, to different velocities). The image in Fig. 1 shows that there are two sources separated by about $80''$ in the north-south direction. Given the positions of the sources, the reduction in amplitude due to primary beam attenuation is estimated to be less than 7 per cent, which is less than the precision of the absolute flux density calibration. This effect can therefore be neglected at 6.7 GHz and no primary beam correction has been applied to either the spectra or the image. These sources in the map in Fig. 1 correspond to two spectral features, a broad one peaking at 7.2 km s^{-1} and

a narrow one peaking at -1.1 km s^{-1} . An inspection of individual planes of the spectral cube confirms that no emission brighter than $0.15 \text{ Jy beam}^{-1}$ is visible at the position of one feature within the velocity range of the other. Both features were detected in the vector averaged spectra constructed separately for each individual observing session, which can be considered as an independent confirmation. Radial velocities in the range $4\text{--}9 \text{ km s}^{-1}$ are typical for the Orion region. The emission from the hot core component peaks in the range $3\text{--}8 \text{ km s}^{-1}$, while the methanol emission core (compact ridge) peaks around $7\text{--}9 \text{ km s}^{-1}$ (Menten et al. 1986; Wright et al. 1996; Cragg et al. 2001). Menten et al. (1988b) found the methanol emission in the southern source peaking at approximately 6 km s^{-1} . However, no methanol emission has been previously reported at or near -1.1 km s^{-1} .

The northern source (the feature peaking at 7.2 km s^{-1}) is located about $10''$ to the south of the IRc2 object. This position is typical for methanol lines at these velocities and is known as the compact ridge (Menten et al. 1988b,c; Wright et al. 1996). From Fig. 1 the source appears extended and two components are readily distinguished. The spectrum also supports this as the profile of the broad feature is asymmetric. To reveal the velocity structure of the source we fitted a Gaussian source model to individual planes of the cube used to construct a cumulative map shown in Fig. 1. The results of these fits are listed in Table 2. The first five columns are the LSR velocity of the channel, the position and the peak flux density of the fitted Gaussian and the total flux density of the source. The last six columns are the Gaussian parameters, the length of the major and minor axes (at half maximum) and the position angle of the major axis, for the fitted Gaussian and the result of deconvolution of the synthesized beam. The uncertainties listed in the table are the formal errors from the Gaussian fit. The formal errors for the deconvolved Gaussians are obtained under assumption that the synthesized beam is known precisely. A good estimate of the actual 1σ positional accuracy is the synthesized beam size divided by the signal to noise ratio in the image (e.g., Fomalont 1999). The noise level in the map of each spectral channel (cumulative map is shown in Fig. 1) is about 20 per cent of maximum. The FWHM of the synthesized beam is $27''.4 \times 10''.2$ and the position angle is $0^\circ.8$, which gives an estimate of the 1σ positional accuracy of $5'' \times 2''$ with the same position angle. Note, however, that for a blended component like $7\text{--}8 \text{ km s}^{-1}$ feature is, the actual accuracy may be worse. The fitted positions in the Table 2 show a trend of moving towards the east as the velocity decreases from 8 km s^{-1} to 7 km s^{-1} . This supports the idea that the source is a blend of two components with similar velocities and positions. The southern source (-1.1 km s^{-1} feature, Fig. 1) is located at the position of the Orion-South region. This region is a known source of methanol emission (Menten et al. 1988b), however, the thermal emission peaks at a velocity of approximately 6 km s^{-1} . The results of the Gaussian fit into the images of different spectral channels across the line profile of the -1.1 km s^{-1} feature are the same within the fitting uncertainty. Therefore, in the Table 2 we listed only one of the fits, corresponding to the peak velocity.

A direct analysis of the visibility data is another, complementary way to obtain information about the source structure. Given a model of the source, this method is able to produce more reliable uncertainties than fitting a deconvolved image. For a weak source, however, one is limited to use the simplest source models only as the ambiguity of the fit increases rapidly with the number of free model parameters. Fig. 2 contains the dependencies of the visibility amplitude on the baseline length for the 7.2 km s^{-1} (upper plot) and -1.1 km s^{-1} features (lower plot). Each point in the plot rep-

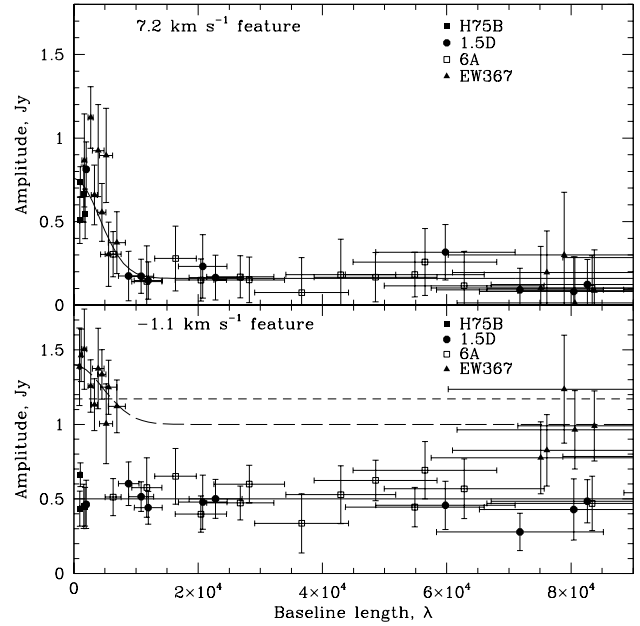


Figure 2. The dependence of the visibility amplitude on the baseline length for 7.2 km s^{-1} (upper plot) and -1.1 km s^{-1} (lower plot) 6.7-GHz features. Different symbols correspond to the data from different array configurations. The solid and dashed lines represent the results of model fitting. The EW367 data for the -1.1 km s^{-1} feature were fitted separately (dashed lines) from the data from other configurations (solid line).

resents a single baseline. Baselines from the different array configurations are shown by different symbols. All visibility data were vector averaged together separately for each baseline using the positions shown in Fig. 1 for the 7.2 km s^{-1} and -1.1 km s^{-1} features respectively, regardless of the projected length. The horizontal error bars in Fig. 2 represent the scatter of the projected length for each baseline. The vertical error bars show the scatter of the averaged amplitude. This complicated scheme of averaging is dictated by the weakness of the source. Different fit results are shown by the solid and dashed lines in Fig. 2. The 7.2 km s^{-1} feature can be described by a symmetric Gaussian source model with a total flux density of $0.6 \pm 0.1 \text{ Jy}$ and FWHM of $18'' \pm 9''$. Taking into consideration that the size of this symmetric model is an average size as the actual source is most probably asymmetric, the value is in agreement with Table 2 (deconvolved sizes and separation between peaks at different velocities). From Fig. 2 the -1.1 km s^{-1} feature appears to have undergone a flare during the EW367 observations (2004 April 10) as the flux densities are significantly different from other configurations (including the 6A observations from 2004 January 5). The solid line represents a point source model with a flux density of $0.5 \pm 0.1 \text{ Jy}$ fitted to all data except that from the EW367 configuration. One can see in Fig. 2 that the -1.1 km s^{-1} feature is unresolved for baseline lengths of about $8 \times 10^4 \lambda$, which implies the source size less than about $2''.6$. The EW367 data were fitted separately. A gradual decrease of the visibility amplitude at the short EW367 baselines seen in Fig. 2 encouraged us to try a two component model, although the point source model is adequate for the data (with the observed noise level an extended component is not necessary to explain the plot). The point source model (short dashed line in Fig. 2) implies the flux density of $1.2 \pm 0.2 \text{ Jy}$. The two component model (long dashed line) includes an unresolved component with the flux density of $1.0 \pm 0.2 \text{ Jy}$ and a symmetric

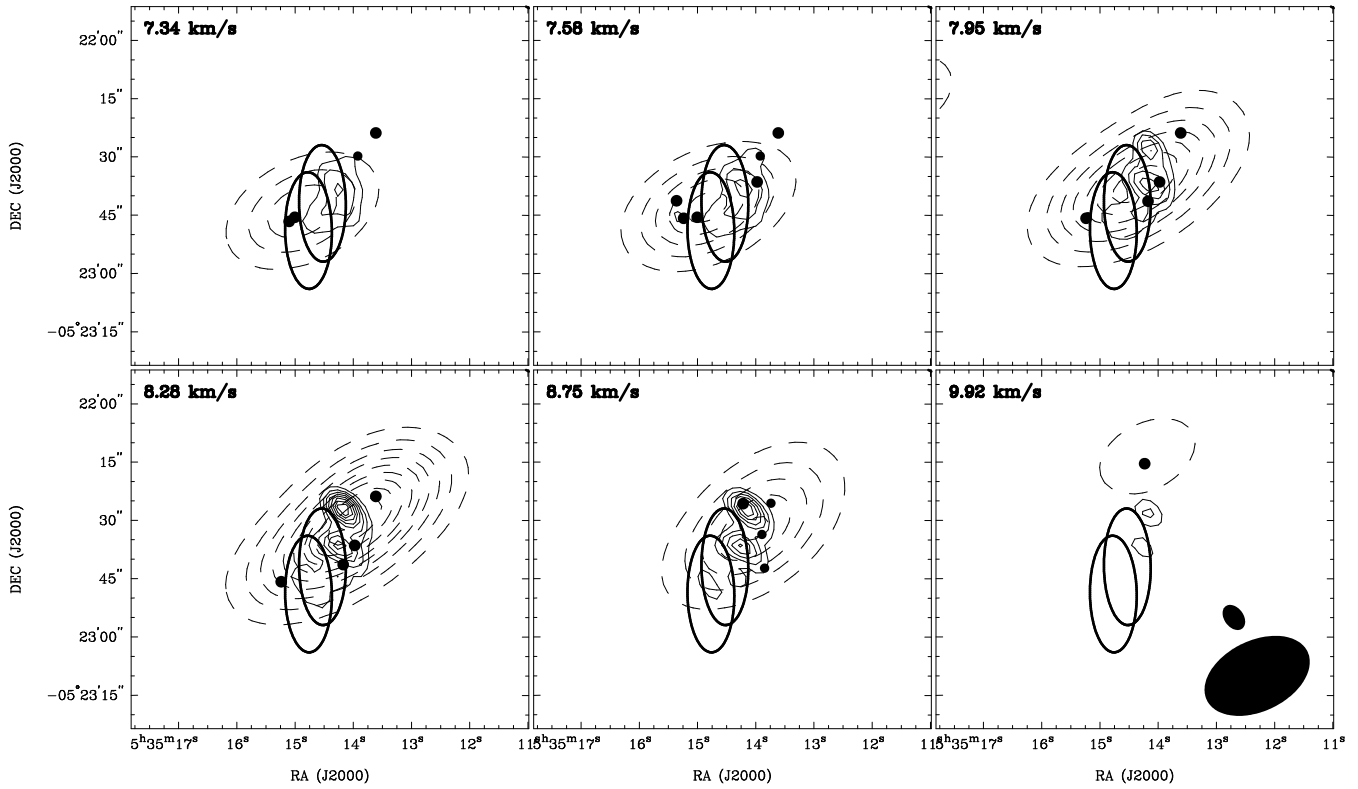


Figure 3. Images of the 25-GHz maser (dashed contours) in OMC-1 at different velocities overlaid on the images of the 95-GHz emission (solid contours) obtained by Wright et al. (1996), courtesy of ADIL. The filled ellipses in the bottom right corner represent the synthesized beams at 25 GHz (large ellipse, $28''.7 \times 18''.1$, -64°) and 95 GHz (small ellipse, 7.1×4.9 , 36°). Contours are 10, 20, 30, 40, 50, 60, 70, 80 and 90 per cent of $86.8 \text{ Jy beam}^{-1}$ at 25 GHz and 20, 30, 40, 50, 60, 70, 80 and 90 per cent of $40.4 \text{ Jy beam}^{-1}$ at 95 GHz. The spectral resolution is 0.5 km s^{-1} and 0.05 km s^{-1} for the 95-GHz data obtained by Wright et al. (1996) and our 25-GHz data, respectively. Bold open ellipses represent the 3σ uncertainty of the 6.7-GHz emission position and correspond to the fit results at 7.2 km s^{-1} and 7.5 km s^{-1} for the left and right ellipse respectively. The filled circles represent 25-GHz maser spots revealed by Johnston et al. (1992). For each subplot, only spots with the peak velocity closer to the subplot velocity than their half width at half maximum plus the width of one VLA spectral channel (0.15 km s^{-1}) are displayed. The circles of a smaller radius correspond to faint 25-GHz spots (less than 10 Jy of the total flux).

Table 3. Results of Gaussian fits to 25-GHz images of characteristic channels shown in Fig.3. All uncertainties are formal errors of the Gaussian fit. A good estimate of the actual 1σ positional accuracy is $2.4'' \times 1.5''$ (full width) with a positional angle of -64° (the synthesized beam has the FWHM of $28.7'' \times 18.1''$ and the same positional angle).

LSR Velocity (km s^{-1})	α_{2000} $5^{\text{h}}35^{\text{m}}$ ($^\circ$)	δ_{2000} $-5^\circ 22'$ ($''$)	Peak flux (Jy)	Total flux (Jy)	Fitted Gaussian			Deconvolved Gaussian		
					maj ($''$)	min ($''$)	PA ($^\circ$)	maj ($''$)	min ($''$)	PA ($^\circ$)
7.34	14.87 ± 0.03	44.0 ± 0.4	35 ± 2	37	29.6 ± 1.1	18.6 ± 0.7	-63 ± 3	7 ± 4	4 ± 3	-50 ± 87
7.58	14.83 ± 0.03	42.8 ± 0.4	48 ± 2	51	30.4 ± 1.2	18.4 ± 0.7	-64 ± 3	10 ± 4	3 ± 4	-64 ± 39
7.95	14.33 ± 0.07	36.5 ± 0.8	68 ± 5	93	38.1 ± 2.8	18.9 ± 1.3	-57 ± 4	25 ± 4	4 ± 6	-51 ± 14
8.28	14.02 ± 0.04	30.9 ± 0.5	89 ± 4	132	40.0 ± 1.6	19.3 ± 0.8	-53 ± 2	28 ± 2	4 ± 4	-46 ± 6
8.75	14.02 ± 0.02	31.8 ± 0.3	45 ± 1	63	35.6 ± 0.9	20.5 ± 0.5	-50 ± 2	22 ± 1	6 ± 2	-35 ± 7
9.92	14.19 ± 0.03	14.0 ± 0.4	14 ± 1	17	29.9 ± 1.3	20.7 ± 0.9	-60 ± 5	11 ± 2	7 ± 5	-5 ± 67

Gaussian source with a total flux density of $0.4 \pm 0.1 \text{ Jy}$ and the FWHM $17'' \pm 13''$. Note, that the flux densities and source sizes in these models are overestimated (less for brighter signals) due to amplitude bias. However, the magnitude of this systematic offset is well below the random noise.

3.2 The 25-GHz data

The 25-GHz methanol maser in OMC-1 was the first maser from the methanol molecule detected in space (Barrett et al. 1971; Chui et al. 1974). Menten et al. (1988c) observed several lines ($J=2$ to 8) in the series and found that maser emission dominates in the spectra for the $J=4$ line and higher while most of the emission in the $J=2$ and 3 transitions is of a thermal (non-maser) nature. Emission was detected from both Orion-KL and Orion-South, resembling the morphology of the source seen in mm-wavelength

methanol lines (Menten et al. 1988b). Johnston et al. (1992) imaged the $J=5$ and 6 masers in the KL region using the VLA D-configuration and showed that the maser consisted of a large number of spots with a small velocity spread, distributed in a $40''$ long crescent shaped region. The spatial resolution of the ATCA in the H75B configuration is much lower than that of the VLA and is comparable with the resolution of the single dish Effelsberg map. Therefore, unlike Johnston et al. (1992) we cannot disentangle any information about individual maser spots and here only attempt to analyze a general picture. From the shape of the spectra on different baselines we have chosen several spectral channels corresponding to the peaks of distinct features. Images of the spectral channels at velocities of 7.34, 7.58, 7.95, 8.28, 8.75, and 9.92 km s^{-1} are shown in Fig. 3. All these images have been corrected for primary beam attenuation. The maser spots revealed by Johnston et al. (1992) at close velocities are overlayed on our 25-GHz image in Fig. 3. For each subplot, we show only those spots, which have peak velocities closer to the subplot velocity than the half width at half maximum determined by Johnston et al. (1992) for these spots plus the width of one spectral channel in the Johnston et al. (1992) data (0.15 km s^{-1}). In Fig. 3 we also show the 95-GHz (the $8_0 - 7_1$ A^+ methanol transition) images sampled at subplot velocities from the spectral cube obtained by Wright et al. (1996), which is available from the NCSA Astronomy Digital Image Library (ADIL)³ and has a spectral resolution of 0.5 km s^{-1} (our 25-GHz data have a spectral resolution of 0.05 km s^{-1}). In a similar manner to the 6.7-GHz data we fitted a Gaussian source model into each spectral channel. The results are listed in Table 3. The columns are the same as for Table 2. As before the uncertainties in the table are formal errors of the Gaussian fit and a good estimate of the actual 1σ accuracy is given by the synthesized beam size and signal to noise ratio, which gives $2.4'' \times 1.5''$ with a positional angle of -64° .

Although we know from the image of Johnston et al. (1992) that the 25-GHz emission contains a larger number of components, these characteristic velocities we show are sufficient to analyze the morphology of the source within the spatial resolution provided by the ATCA. Menten et al. (1988c) also found 6 components in their Effelsberg data, which has a comparable spatial resolution to our measurement. However, the component velocities listed by Menten et al. (1988c) are slightly different. Moreover, our data imply the presence of a 7.58 km s^{-1} feature, which is not listed by Menten et al. (1988c), but do not require a 9.6 km s^{-1} feature detected by them. The difference is most probably due to the interferometric nature of our measurement as the output signal for a complex source depends on the size of individual baseline and its orientation with respect to the source. Another plausible explanation of the difference is temporal variability in the source. The image of Johnston et al. (1992) does not contain a spot at or near 9.6 km s^{-1} .

A comparison of our 25-GHz image with the maser spots of Johnston et al. (1992) in Fig. 3 (see also Table 3) shows that they are in general agreement. However, the south-eastern group of maser spots dominates in our image at low velocities. The most north-western spot in the 7.34- km s^{-1} subplot in Fig. 3 is, therefore, weak according our data. This is the spot number 11 in Table 2 of Johnston et al. (1992). This spot is the brightest spot observed (total flux 92 Jy) and is rather broad in the velocity domain (peak is at 8.0 km s^{-1} , half peak linewidth is 1.03 km s^{-1}). Therefore, we suspect that significant temporal variations have occurred in the 25-GHz masers since the observations of Johnston et al. (1992).

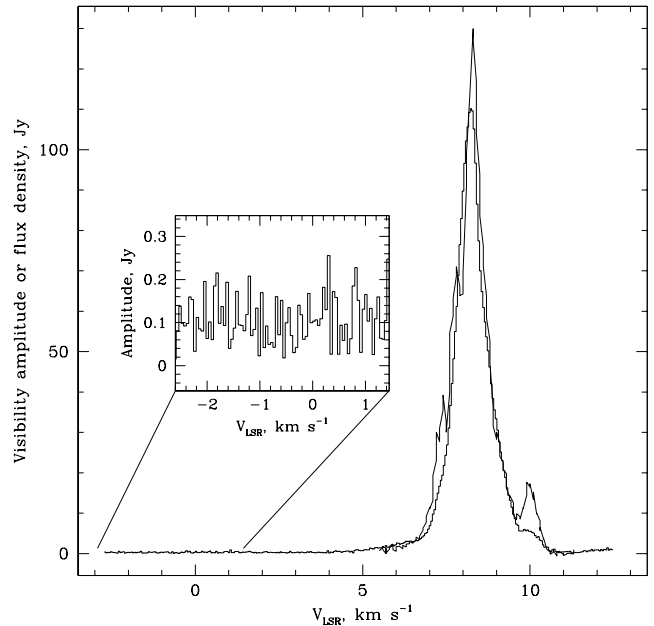


Figure 4. The spectrum scaled to correct for the primary beam attenuation and the spectrum of the image flux density (bold line) of the 25-GHz maser in OMC-1. The subplot shows the 25-GHz spectrum at the position of the 6.7-GHz emission near -1 km s^{-1} . The scaling factors are 2.71 for the main plot and 1.16 for the subplot.

The vector averaged spectrum of the 25-GHz emission is shown in Fig. 4. The data on all baselines except those including the CA06 antenna, were vector averaged together for the position $\alpha_{2000} = 5^{\text{h}} 35^{\text{m}} 14^{\text{s}}.02$, $\delta_{2000} = -5^{\circ} 22' 30''.9$, which corresponds to the peak of the 25-GHz emission in the image (Fig. 3) at 8.28 km s^{-1} . The amplitude was scaled by a factor of 2.71 to account for primary beam attenuation at the offset of the above mentioned position with respect to the pointing centre. However, this method of correcting for the primary beam is valid only for a point source. In a complex source the spots, which lie closer to the pointing centre than the above mentioned position, will appear brighter, while the effect of the spots which lie further will be underestimated. Moreover, the measured flux density is very sensitive to the pointing errors when the source is offset from the pointing centre. The magnitude of this effect is determined by the derivative of the primary beam and results in an error of 17–39 per cent (at the position of the 25-GHz peak) if a pointing error of $5\text{--}10''$ is assumed. The impact of the pointing errors on the measured flux density for a complex extended source can be alleviated by proper mosaicing observations. Another way to obtain a spectrum of the source from interferometric data is to sum the flux density in the deconvolved image for each spectral channel. This enables a proper primary beam correction to be done, taking into account the different positions of individual features and produces a single dish-like spectrum where the individual spectral features are emphasized. However, this method includes a non-linear deconvolution algorithm, which makes it difficult to analyze the noise and to assess whether a feature in the spectrum is reliable. In addition, in the case of a poor uv-coverage the quality of such spectrum is limited by the dynamic range of the image (5:1 in our 25-GHz measurement) and the absolute noise level is different at the line centre and at the wings. Freedom in the choice of the image region where pixel values are summed and the fact that the values of adjacent pixels

³ Accessible via URL <http://imaginglib.ncsa.uiuc.edu>

usually correlate make this method inappropriate for weak signals like the 6.7-GHz line discussed in the previous section. However, such a spectrum can be constructed for the 25-GHz maser which is bright. The spectrum obtained by summing over a $100''$ square centered at $\alpha_{2000} = 5^h 35^m 14^s.33$, $\delta_{2000} = -5^\circ 23' 14''.6$ is shown in Fig. 4 by the bold line. The size and position of the image region involved in summation is chosen to accommodate all the emission seen in Fig. 3 and to avoid as far as possible the region near the edge of the field of view where the noise of deconvolution algorithm is amplified by the primary beam correction procedure. The most significant difference between this spectrum and the vector averaged one is near 10 km s^{-1} . This is because the source is offset to the north at these velocities (see Fig. 3) and the primary beam correction uses the position of the peak at 8.28 km s^{-1} (see the discussion above). The spectrum resembles that of Johnston et al. (1992) obtained using the same method, although our spectrum peaks at 8.28 km s^{-1} , while that of Johnston et al. (1992) peaks at about 7.9 km s^{-1} , and an additional feature near 7.6 km s^{-1} seems to be present in our spectrum. These differences can be explained by both the errors resulting from the dynamic range and the pointing inaccuracy as well as by different uv-coverage in the two experiments. Temporal variability of the maser is another possible explanation. The peak flux density determined using both the vector averaged spectrum and the image flux spectrum is in agreement with observations of Johnston et al. (1992) and Menten et al. (1988c) within the accuracy of our measurement.

Menten et al. (1988c) report 25-GHz methanol emission from the Orion-South region (southern 6.7-GHz source) for the $J=2, 3$ and 4 lines in the series. The source has also mm-wavelength methanol line emission peaking at 6 km s^{-1} (Menten et al. 1988c). However, no methanol emission at -1.1 km s^{-1} has been reported. The subplot in Fig. 4 shows the 25-GHz vector averaged spectrum at velocities near -1.1 km s^{-1} . As for the main plot, all data except those resulting from the baselines with the CA06 antenna were vector averaged together. However, for the subplot in Fig. 4 the position of the averaging centre was $\alpha_{2000} = 5^h 35^m 13^s.93$, $\delta_{2000} = -5^\circ 24' 05''.3$, which correspond to the position determined for the 6.7-GHz emission at -1.1 km s^{-1} (Fig. 1). The pointing centre was much closer to this position and, therefore, a smaller primary beam correction factor of 1.16 has been applied. The flux density of the $5_2 - 5_1$ E emission at 25 GHz near the velocities of -1.1 km s^{-1} is below the detection limit. The rms noise (1σ) is 0.12 Jy.

4 DISCUSSION

4.1 Temporal variability and previous observations

The non-imaging analysis discussed in 3.1 shows that the -1.1 km s^{-1} feature was stronger in the EW367 data (2004 April 10) with respect to the data from other array configurations. This difference is unlikely to be due to instrumental effects. The derived secondary calibrator flux densities at 6.7-GHz are 0.68 Jy, 0.87 Jy, 0.87 Jy, and 1.07 Jy for the 2003 June 9–10 (H75B), 2003 November 12 (1.5D), 2004 January 5 (6A), and 2004 April 10 (EW367) observations, respectively. These numbers imply that the precision of the absolute calibration is better than 16 per cent. Although the secondary calibrator appears brighter in the EW367 data, the difference in the flux density is not enough to explain the -1.1 km s^{-1} feature being 2–3 times stronger in these data. In addition, there is a good agreement between the amplitudes on short and long baselines of the same session (Fig. 2). Hence, a difference in the phase

stability at different dates is unlikely to explain the observed difference of amplitudes (a vector averaging of the data is used before the amplitudes are calculated) because the decorrelation should be stronger on longer baselines. A final argument against instrumental effects is an agreement between the 7.2 km s^{-1} feature data from the different array configurations. Therefore, it is likely that the -1.1 km s^{-1} feature had a flare in April 2004.

The first observations of the OMC-1 at 6.7 GHz were carried out by Caswell et al. (1995) on 1992 December 17–24 using the Parkes 64-m telescope. The telescope was pointed towards $\alpha_{2000} = 5^h 35^m 14^s.35$, $\delta_{2000} = -5^\circ 22' 24''.4$. A weak (0.5 Jy) feature at 7 km s^{-1} was reported. The detection limit was about 0.3 Jy (Caswell et al. 1995). So the flux density measured more than a decade ago at Parkes for the 7.2 km s^{-1} feature is in good agreement with our ATCA observations (see Table 2). The Parkes spectrum (Caswell, priv. comm.) shows an absorption feature at 4–7 km s^{-1} , which is not present in our data. This absorption obscures the red wing of the emission feature and is probably resolved by the ATCA. The Parkes spectrum also contains a hint on the -1.1 km s^{-1} feature at the level of 0.2 Jy. According to our measurement (Table 2) the -1.1 km s^{-1} feature is located approximately $1'.6$ to the south from the position observed by Caswell et al. (1995). Such an offset implies a beam attenuation factor of 2, assuming the half-power beamwidth of $3'.3$ at 6.7 GHz. If the flux density of the -1.1 km s^{-1} feature was 0.5 Jy as we had in all sessions except April 10 (Fig. 2), the attenuated flux density would be in agreement with the observations of Caswell et al. (1995).

The C425 project from the ATCA archive was devoted to search for methanol masers at 6.7 GHz in proplyds in the Orion nebula. The observations were carried out on 1995 January 6 and March 30 using the 6A and 1.5A array configurations respectively. The phase and pointing centre was at $\alpha_{2000} = 5^h 35^m 0^s$, $\delta_{2000} = -5^\circ 23' 0''$, which is about $3'.7$ away from the positions of the 6.7-GHz emission we have measured (Table 2). The offset of $3'.7$ implies a factor of 2 attenuation due to the primary beam. We processed these data the same way as our 6.7-GHz observations and created spectra similar to Fig. 1. The amplitudes were scaled to correct for the primary beam attenuation. Neither the -1.1 km s^{-1} feature, nor the 7.2 km s^{-1} were detected in the January 6 data which had a typical 1σ single baseline amplitude rms of about 0.2 Jy. From the calibrator data we suspect serious technical problems during this session. The March 30 data suffer from poor phase stability, however, both spectral features are clearly present in the data. The 7.2 km s^{-1} feature has an amplitude of about 0.6 ± 0.2 Jy on the shortest baselines, which is in agreement with our measurement (Table 2, Fig. 1 and 2). The -1.1 km s^{-1} feature has an amplitude of about 0.2 ± 0.1 Jy and is revealed only if all baselines are averaged together. This value is much lower than the flux density of about 0.5 Jy expected from our observations, although it is underestimated because baselines of different lengths have been averaged together and the phase stability was bad. However, we cannot exclude the possibility that the -1.1 km s^{-1} feature was really fainter in 1995, than in 2003, as we have observed it to be variable on a timescale of months.

4.2 The 6.7-GHz emission at 7–8 km s^{-1}

Inspection of Tables 2 and 3 as well as Figure 3 show that the 6.7-GHz emission at 7–8 km s^{-1} is coincident with the 25-GHz emission detected in our observations within the uncertainty of the measured positions. The tendency to move to the east for lower velocity exists for the transitions at both frequencies. In Fig. 3 we

overlayed the 25-GHz spots found by Johnston et al. (1992), which have more accurate positions than our measurement but were observed 15 years earlier. Also superimposed are the 95-GHz image obtained by Wright et al. (1996) and 3σ error ellipses showing the positions of the 6.7-GHz emission at 7.2 km s^{-1} , and 7.5 km s^{-1} . It is clear from Fig. 3 that both components of the $7\text{--}8 \text{ km s}^{-1}$ feature may be associated with 25-GHz spots, although the agreement is better for the 7.2-km s^{-1} component (left ellipse in Fig 3) in terms of both position and velocity. This component is likely to be associated with the south-eastern tip of the crescent shaped region traced by the 25-GHz maser spots. The uncertainty ellipse for the 7.5-km s^{-1} component may include the southern peak at 95-GHz. Although the coarse spectral resolution in the data of Wright et al. (1996) makes this comparison difficult. The $7\text{--}8 \text{ km s}^{-1}$ feature consists of at least two components emanating from close locations. In this case the Gaussian fit may suggest the positions of these components to be closer together than they are in reality. Therefore, the actual agreement may even be better. The source is too complex to determine any definite association with the spatial resolution of our 6.7-GHz data, but the general coincidence with the area containing 25-GHz and 95-GHz emission is obvious. A high resolution study is required to measure the position of the 6.7-GHz emission with respect to individual 25-GHz maser spots. However, it is difficult to do this with existing interferometers because the source is very weak at 6.7 GHz and most probably resolved.

It is clear from Fig. 3 that the coincidence between 25-GHz maser spots revealed by Johnston et al. (1992) and the peaks of the 95-GHz emission detected by Wright et al. (1996) is good, but not perfect. It seems unlikely that this small discrepancy is due to positional errors. Most probably, the 25-GHz masers require more specific physical conditions than the 95-GHz masers. The bright masers at 25-GHz are relatively rare (Menten et al. 1986), while 95-GHz masers are common (e.g., Val'ts et al. 2000). Another possible explanation is temporal variability of the 25-GHz emission suspected in section 3.2. It is worth noting, that the nature of the 95-GHz emission in OMC-1 is not completely clear. This is a well known class I maser transition (e.g., Val'ts et al. 2000) and Plambeck & Wright (1988) concluded on the basis of the brightness temperature that at least a part of the 95-GHz emission in OMC-1 is due to a maser action. However, the limit on the brightness temperature ($T_b > 500 \text{ K}$) set by Plambeck & Wright (1988) is not strong and higher spatial resolution observations are required to answer the question unambiguously. A comparison of interferometric images of the 25-GHz and 95-GHz masers with that of various outflow and dense molecular gas tracers shown that these masers arise in the interface regions where outflows interact with the ambient material (Johnston et al. 1992; Plambeck & Menten 1990). Therefore, the $7\text{--}8 \text{ km s}^{-1}$ feature is likely to emanate from the same volume of gas disturbed by the outflow, even if there is no co-existence with the 25-GHz maser spots at finer scales.

At present we cannot definitively discriminate whether the observed 6.7-GHz line peaking at 7.2 km s^{-1} is a maser or has a quasi-thermal nature (i.e., the level populations of the 6.7-GHz transition are without inversion). The straightforward approach to estimate the brightness temperature limit using the fit result at either velocity listed in Table 2 gives a brightness temperature of about 40 K. Because the feature definitely is resolved by our observations, this value is a rough estimate of the average brightness temperature and should always be considered as a lower limit to the actual brightness temperature.

4.3 Co-existence of masers belonging to different classes

In the previous section we have shown that the 6.7-GHz (class II maser transition) emission feature peaking at 7.2 km s^{-1} is likely to arise from the region where the 25 GHz masers are (class I). The spatial resolution of our data is too coarse to be able to claim that exactly this is realized in such a complex source as OMC-1, although there is agreement within the positional uncertainty of our measurement. This is a new finding because, as mentioned above, methanol masers of different classes co-existing in the same star-forming region are usually situated at considerably different locations in the source.

In this section we address the possibility of coincidence of the different class maser locations in the strict theoretical sense: whether there is a pumping regime allowing a simultaneous inversion of transitions belonging to different classes in the same volume of gas? Previous studies show that this is possible in principle. For example the class I $11_2 - 11_1 \text{ E}$ transition at 26.3 GHz is present in the list of class II methanol maser candidates of Sobolev et al. (1997b). However, the existence of inversion in class II maser transitions under conditions where class I masers are strong has not been seriously considered, though it was briefly mentioned in the conference proceedings by Voronkov et al. (2005).

Pumping analysis has shown that the dust temperature of the maser environment is one of the key parameters which determines the relative strength of the different types of methanol maser transitions. When the dust temperature is high ($T > 120 \text{ K}$) the radiative excitation from the ground to the second torsional state becomes influential and controls the populations of the masing transitions. The levels of the first and the second torsionally excited states are located 350–650 K and 600–800 K above the levels of the ground state, respectively (Mekhtiev, Godfrey & Hougen 1999). Therefore, the corresponding transitions occur at $(0.6 - 1.3) \times 10^{13} \text{ Hz}$ ($20 - 40 \mu\text{m}$) and $(1.2 - 1.7) \times 10^{13} \text{ Hz}$ ($15 - 25 \mu\text{m}$). The strong class II masers appear when the dust temperature is sufficiently high ($T > 150 \text{ K}$) and the gas temperature is lower or about the same (Sobolev & Deguchi 1994; Sobolev et al. 1997a). Calculations have shown that the strong class I masers do not appear when the distribution of population numbers is controlled by radiative processes in transitions between the ground and the second torsionally excited state. The situation changes only for rather high densities (exceeding 10^8 cm^{-3}) which are not likely to occur in methanol maser sites.

The situation at lower temperatures was considered by Cragg et al. (1992). This work was limited to the case where conditions in the masing region are such that the radiative transitions between different torsionally excited states are not influential. This implies dust temperatures below 50 K. Cragg et al. (1992) have shown that the class I maser transitions are considerably inverted only when the gas temperature exceeds that of the ambient radiation, i.e., excitation processes are dominated by collisions with the gas. The class II masers appear only when the radiative excitation prevails. So situations where the 6.7-GHz transition can attain considerable inversion in the star forming region simultaneously with the strong class I masers, are limited to cases where the dust temperature is in the range between 50 K to 120 K and the gas temperature has a similar value.

We considered a set of models where the dust responsible for the pumping is intermixed with the gas within the molecular cloud. The dust temperature was varied over the range 50 K to 260 K. Figure 5 displays the results of calculations for models with different dust (T_{dust}) and gas (T_{gas}) temperatures, which were assumed

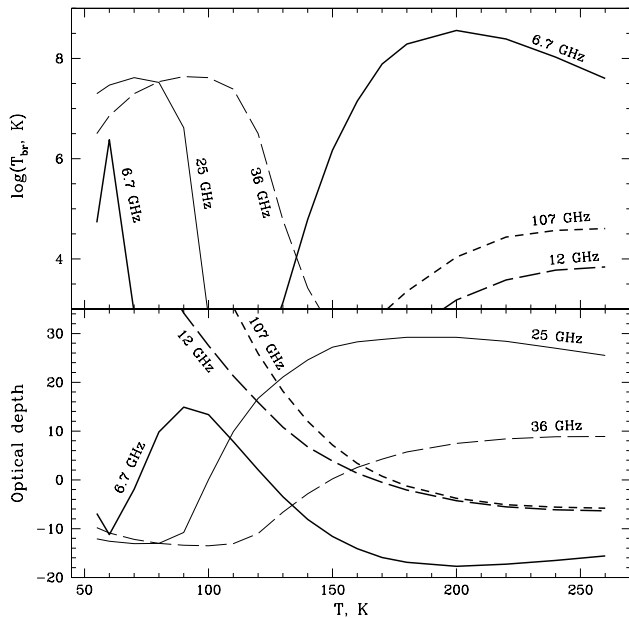


Figure 5. The model dependence of the brightness temperature and optical depth of various methanol maser transitions on the temperature ($T = T_{gas} = T_{dust}$). Bold lines represent class II transitions.

to be equal. This is a good approximation for regions with density and temperature in the range typical for the 25-GHz masers (see, e.g., Sobolev, Watson & Okorokov 2003), which appear after the passage of a moderate shock (e.g., Whitworth & Clarke 1997). Outlines of the code are described in Sutton et al. (2004) and further details can be found in Sobolev et al. (1997a,b) and Köppen & Kegel (1980). The main difference from the modelling procedure described in Sobolev et al. (1997b) is that the new calculations take into account radiative processes on the dust which is intermixed with the gas within the source, and the external radiation is reduced to the microwave background with $T_{bg} = 2.7$ K. The cloud models presented have the following parameters: the hydrogen number density is 10^5 cm^{-3} , the specific (per unit of the linewidth) methanol column density is $10^{12} \text{ cm}^{-3} \text{ s}$, and the beaming factor (ϵ^{-1}) is 10. For all models shown here the optical depth of the dust in the source is set to be proportional to the square of the frequency and assumed to be equal to 0.5 at 10^{13} Hz ($30 \mu\text{m}$). The dependence of the brightness temperature and optical depth in different transitions versus the temperature ($T = T_{gas} = T_{dust}$) is shown in Fig. 5. A maser line is expected to have a high brightness temperature and a negative optical depth. Increasing the temperature (T) in such a cloud changes the balance of excitation processes in favour of radiative ones. So, the expectation is that the class I masers should appear at low temperatures while at high temperatures the class II masers should shine brightly. The transitions all show a single smooth change from non-masing to masing condition (positive to negative optical depth), with the notable exception of the 6.7-GHz transition. The secondary masing regime of the 6.7-GHz transition is at low temperature (60 K), overlapping with the regime favouring the class I 25-GHz masers. This is a new pumping regime, which is not expected in the traditional methanol maser classification scheme.

To investigate this regime further, we repeated calculations for a single temperature $T = T_{dust} = T_{gas} = 60$ K using a modified energy level diagram. We deliberately excluded the energy levels

Table 4. Optical depths of selected transitions for various models. For all models $T=60$ K. The first 3 models involve the dust intermixed with the gas in the cloud (I), the last 3 models involve an external isotropic layer of dust (E).

Model	1	2	3	4	5	6
Dust	I	I	I	E	E	E
$v_t = 1$	yes	yes	no	yes	yes	no
$v_t = 2$	yes	no	no	yes	no	no

Frequency GHz	Optical depths					
6.7	-15.7	-16.6	142	18.1	-11.5	139
12	68.3	68.9	192	100	116	195
25	-12.7	-12.9	-10.8	-11.6	-11.8	-10.8
36	-11.3	-11.3	-10.5	-10.4	-10.7	-10.5
44	77.1	89.6	-8.9	21.9	49.9	-8.9
95	101	113	-1.0	49.8	72.0	-1.0
107	48.0	33.6	192	49.8	61.5	190

of the torsionally excited states of the methanol molecule to check their influence on the overall pumping. In addition, in some models we simulated the pumping by an external dust layer as it was done by Sobolev et al. (1997b). For these models an isotropic distribution of the dust emission was assumed (i.e. the dilution factor is 1). All other parameters were the same as in the models used to produce Fig. 5. More detailed analysis require a comprehensive investigation of the vast parameter space and will be reported elsewhere. The optical depths of selected transitions obtained in these models are listed in Table 4. The first model corresponds to the $T = 60$ K point in Fig. 5. Table 4 shows that the 6.7-GHz transition is inverted only if the first torsionally excited state is included. Addition of the second torsionally excited state does not significantly affect the result, except for model 4 involving an external dust layer. This means that the pumping of the 6.7-GHz transition in this low temperature regime is going through the levels of the first torsionally excited state in contrast to the pumping of the bright class II masers, which requires both the first and second torsionally excited states (Sobolev & Deguchi 1994). In the models where the dust is intermixed with gas (labelled I in Table 4), the 6.7-GHz transition is inverted stronger (greater optical depth by absolute value) than in the case of the external dust (labelled E in Table 4). In model 4, which includes both the first and the second torsionally excited states and simulates the pumping by an external dust layer, the 6.7-GHz transition is not inverted. Therefore, it is essential that the dust is intermixed with the gas for this low temperature mechanism to be realized in practice. There is no significant difference between the optical depths in the class I maser transitions at 25 GHz and 36 GHz in these models. This means that these transitions are pumped mostly through the levels of the ground torsional state of the molecule. For the given values of the fixed model parameters, the transitions at 44 GHz and 95 GHz are not inverted if at least one torsionally excited state is included. These transitions belong to the $(J+1)_0 - J_1 A^+$ transition series ($J=6$ and 7 , respectively), which occurs between the same K-ladders as the $5_1 - 6_0 A^+$ transition at 6.7 GHz, but in the opposite directions. Therefore, the tendency for 6.7 GHz to invert due to the pumping through the levels of the first torsionally excited state reduces the inversion of the $(J+1)_0 - J_1 A^+$ transitions. Finding the right balance between these processes requires a detailed study of the parameter space.

4.4 The -1.1 km s^{-1} feature at 6.7 GHz

According to position listed in the Table 2, the -1.1 km s^{-1} feature at 6.7 GHz originates in the Orion-South region, which contains a prominent dust and NH_3 condensation (Keene, Hildebrand & Whitcomb 1982; Batrla et al. 1983). However, the feature is noticeably blue-shifted with respect to the normal spread of velocities for lines tracing this molecular core and no emission in methanol lines has been previously reported in Orion-South at this velocity (see, e.g., Tatematsu et al. 1993; Menten et al. 1988b). The source appears to be unresolved (Table 2) which implies an angular size less than $5'' \times 2''$ and a brightness temperature greater than about 1400 K. The non-imaging analysis of the visibility data described in 3.1 yields the size less than $2''6$ (a fit for all data except that from the EW367 array configuration), and thus the brightness temperature greater than about 2000 K. This high brightness temperature and peculiar velocity of the feature indicate that the detected line most probably is a maser. The feature appears to show temporal variability (see section 3.1), which is another indicator that it is likely a maser and not quasi-thermal.

Sensitive observations in the infrared and radiocontinuum (Zapata et al. 2004; O'Dell & Doi 2003) do not show the presence of a compact source at the peak position of the newly detected methanol maser listed in the Table 2. However, positional uncertainties of our observations do not allow us to rule out the possibility of association with 1.3 cm sources 139-409 and 140-410 of Zapata et al. (2004). The nature of these sources is unclear and they may be sources of gyrosynchrotron emission or ionized outflows from low-mass stars (Zapata et al. 2004).

It is likely that the methanol maser in Orion-South is associated with the outflow. Schmid-Burgk et al. (1990) detected a CO outflow presumably ejected from the CS3/FIR4 infrared source. The CS3 and FIR4 positions may actually represent the same object observed in the CS line and 1.3 mm continuum, respectively. The nominal separation between them is $5''5$ along the outflow axis (Schmid-Burgk et al. 1990). The receding part of the outflow is a remarkable $120''$ long jet with a very narrow width ($8''$). The approaching part of the outflow appears on the other side of CS3/FIR4 and has an irregular shape covering the whole Orion-South region. The component is seen at velocities from 0 to 3 km s^{-1} and encompasses the methanol maser location. Schmid-Burgk et al. (1990) argued that this component of the outflow might protrude into the HII region M42, which could explain its ill-defined appearance. Observations of SiO lines tracing dense parts of the outflow display blue wings spanning down to -5 km s^{-1} (Ziurys, Wilson & Mauersberger 1990). The position of the methanol maser at -1.1 km s^{-1} coincides with the blueshifted SiO emission within the uncertainty of the measurement (Table 2 and Ziurys et al. 1990). It is therefore possible, that the maser is associated with the approaching part of the outflow from CS3/FIR4.

It should be mentioned that the Orion-South region contains several outflows (see, e.g., O'Dell & Doi 2003) possibly originating from the young stellar objects whose formation was induced by outflow described in Schmid-Burgk et al. (1990). Observations of H_2O masers (Gaume et al. 1998) and HH objects (O'Dell & Doi 2003) show that outflows in the region are quite rapid and the velocity of the newly detected 6.7-GHz methanol maser line component is well within their velocity spread. At present it is not possible to associate this methanol maser with any particular outflow or young stellar object. Another weak 6.7-GHz methanol maser probably associated with an outflow has been found towards NGC 2024

(source FIR4) by Minier et al. (2003). Though NGC 2024 is situated rather far from Orion-South (about 4° to the north) it also belongs to the Orion complex.

The excitation analysis of Sobolev et al. (1997a) shows that class II methanol masers can be situated at considerable distances from the young stellar object if the associated region is affected by an outflow which releases methanol from the icy dust grain mantles and warms up the dust in the maser vicinity. Great enhancement of the methanol abundance at the edges of the outflows is confirmed observationally (see, e.g., Bachiller et al. 1995, 1998; Gibb & Davis 1998). Association of a considerable portion of class II methanol masers with outflows is supported by statistics (see, e.g., Malyshev & Sobolev 2003; Codella et al. 2004) and observations of particular sources (see, e.g., De Buizer et al. 2002; Minier et al. 2003). We are currently unable to reveal whether these weak masers found in the Orion complex are pumped via a low temperature mechanism similar to that described in 4.3 or by the standard scheme (Sobolev & Deguchi 1994; Sobolev et al. 1997a,b) using the hot dust emission from a nearby source. According to the position listed in Table 2, the -1.1 km s^{-1} maser is associated with the southern tip of the dust condensation in Orion-South (Mezger, Wink & Zylka 1990). The bulk of the dust in this region is rather cold ($T < 70 \text{ K}$) to allow the pumping via the standard scheme (Mezger et al. 1990; Mookerjee et al. 2000). However, condensations with significantly enhanced dust temperatures ($\approx 200 \text{ K}$) do exist (e.g., Mezger et al. 1990). Due to the lack of the dust temperature maps at high spatial resolution, it is impossible to discriminate between the pumping regimes on the basis of the dust temperature. We detected no 25-GHz emission towards the position of the 6.7-GHz maser in Orion-South. Therefore, if the low temperature mechanism is realized, the parameters are unlikely the same as used in 4.3. Sensitive observations of the other methanol and hydroxyl maser transitions toward 6.7-GHz maser positions in Orion-South and NGC 2024 may elucidate physical status of these sources.

5 CONCLUSIONS

- (i) Two 6.7-GHz methanol emission features have been detected towards OMC-1, one narrow feature with a peak at -1.1 km s^{-1} and a broad feature with a peak at 7.2 km s^{-1} .
- (ii) The 7.2 km s^{-1} feature consists of at least 2 components which are close in both position and velocity. These components are likely to be associated with the outflow traced by the 25-GHz masers and 95-GHz emission.
- (iii) There is a pumping regime which produces a weak 6.7-GHz maser (class II) simultaneously with the 25-GHz masers (class I) for relatively low dust temperatures ($T \approx 60 \text{ K}$). The pumping occurs through the levels of the first torsionally excited state and is due to the emission of dust intermixed with gas. Brightness temperatures of the order of 10^6 K can be achieved for such masers.
- (iv) The -1.1 km s^{-1} feature is most probably a maser with a brightness temperature $> 1400 \text{ K}$. It originates in the Orion-South region and may be associated with the approaching part of the outflow seen in CO. This feature is most probably variable.
- (v) No $5_2 - 5_1 \text{ E}$ 25-GHz emission has been detected towards the Orion-South region at velocities near -1 km s^{-1} .

ACKNOWLEDGMENTS

We would like to thank the local staff of the Narrabri Observatory, and particularly Robin Wark, Bob Sault and Mark Wieringa, for the help during observations shortly after the new 12-mm system has become available at the ATCA and for numerous useful advises during the data processing stage. We greatly appreciate the efforts of James Caswell for the internal refereeing of the first version of manuscript. The Australia Telescope is funded by the Commonwealth of Australia for operation as a National Facility managed by CSIRO. The authors would like to thank the NCSA Astronomy Digital Image Library (ADIL) for providing 95-GHz images obtained by Wright et al. (1996) for this article. MAV was partially supported by the RFBR grants no. 98-02-16916 and no. 01-02-16902 and by the program "Extended objects in the Universe-2003". AMS and ABO were supported by the RFBR grant no. 03-02-16433. SPE acknowledges financial support for this work from Australia Research Council.

REFERENCES

- Argon A. L., Reid M. J., Menten K. M., 2003, *ApJ*, 593, 925
 Bachiller R., Liechti S., Walmsley C. M., Colomer F., 1995, *A&A*, 295, L51
 Bachiller R., Codella C., Colomer F., Liechti S., Walmsley C. M., 1998, *A&A*, 335, 266
 Batrla W., Wilson T. L., Bastien P., Ruf K., 1983, *A&A*, 128, 279
 Barrett A. H., Schwartz P. R., Waters J. H., 1971, *ApJ*, 168, L101
 Breckenridge S. M., Kukolich S. G., 1995, *ApJ*, 438, 504
 Caswell J. L., Vaile R. A., Ellingsen S. P., Whiteoak J. B., Norris R. P., 1995, *MNRAS*, 272, 96
 Chui M. F., Cheung A. C., Matsakis D., Townes C. H., Cardasmenos A. G., 1974, *ApJ*, 187, L19
 Codella C., Lorenzani A., Gallego A. T., Cesaroni R., Moscadelli L., 2004, *A&A*, 417, 615
 Cragg D. M., Johns K. P., Godfrey P. D., Brown R. D., 1992, *MNRAS*, 259, 203
 Cragg D. M., Sobolev A. M., Ellingsen S. P., Caswell J. L., Godfrey P. D., Saliu S. V., Dodson R. G., 2001, *MNRAS*, 323, 939
 De Buizer J. M., Walsh A. J., Piña R. K., Phillips C. J., Telesco C. M., 2002, *ApJ*, 564, 327
 Ellingsen S. P., von Bibra M. L., McCulloch P. M., Norris R. P., Deshpande A. A., Phillips C. J., 1996, *MNRAS*, 280, 378
 Ellingsen S. P., 2005, *MNRAS*, 359, 1498 (astro-ph/0503308)
 Fomalont E. B., 1999, in Taylor G., Carilli C., Perley R., eds, *ASP Conf. Ser. Vol. 180, Synthesis imaging in radio astronomy II*. Astron. Soc. Pac., San Francisco, p. 301
 Gaume R. A., Wilson T. L., Vrba F. J., Johnston K. J., Schmid-Burgk J., 1998, *ApJ*, 493, 940
 Genzel R., Stutzki J., 1989, *ARA&A*, 27, 41
 Gibb A. G., Davis C. J., 1998, *MNRAS*, 298, 644
 Johnston K. J., Gaume R., Stolovy S., Wilson T. L., Walmsley C. M., Menten K. M., 1992, *ApJ*, 385, 232
 Keene J., Hildebrand R. H., Whitcomb S. E., 1982, *ApJ*, 252, L11
 Köppen J., Kegel W. H., 1980, *A&AS*, 42, 59
 Lovas F. J., *J. Phys. Chem. Ref. Data*, 1992, 21, 181
 Malyshev A. V., Sobolev A. M., 2003, *A&AT*, 22, 1
 Minier V., Conway J. E., Booth R. S., 2001, *A&A*, 369, 278
 Minier V., Ellingsen S. P., Norris R. P., Booth R. S., 2003, *A&A*, 403, 1095
 Mekhtiev M. A., Godfrey P. D., Hougen J. T., 1999, *J. Molec. Spectrosc.*, 194, 171
 Menten K. M., 1991a, in Haschick A. D., Ho P. T. P., eds, *Proc. of the Third Haystack Observatory Meeting*, p. 119
 Menten K. M., 1991b, *ApJ*, 380, L75
 Menten K. M., Walmsley C. M., Henkel C., Wilson T. L., 1986a, *A&A*, 169, 271
 Menten K. M., Walmsley C. M., Henkel C., Wilson T. L., 1986b, *A&A*, 157, 318
 Menten K. M., Walmsley C. M., Henkel C., Wilson T. L., 1988a, *A&A*, 198, 253
 Menten K. M., Walmsley C. M., Henkel C., Wilson T. L., 1988b, *A&A*, 198, 267
 Mezger P. G., Wink J. E., Zylka R., 1990, *A&A*, 228, 95
 Mookerjee B., Ghosh S. K., Rengarajan T. N., Tandon S. N., Verma R. P., 2000, *AJ*, 120, 1954
 O'Dell C. R., Doi T., 2003, *AJ*, 125, 277
 Plambeck R. L., Wright M. C. H., 1988, *ApJ*, 330, 61
 Plambeck R. L., Menten K. M., 1990, *ApJ*, 364, 555
 Schmid-Burgk J., Güsten R., Mauersberger R., Schulz A., Wilson T. L., 1990, *ApJ*, 362, L25
 Slysh V. I., Kalenskii S. V., Val'tts I. E., Otrupcek R., 1994, *MNRAS*, 268, 464
 Sobolev A. M., Deguchi S., 1994, *A&A*, 291, 569
 Sobolev A. M., Cragg D. M., Godfrey P. D., 1997a, *A&A*, 324, 211
 Sobolev A. M., Cragg D. M., Godfrey P. D., 1997b, *MNRAS*, 288, L39
 Sobolev A. M., Watson W. D., Okorokov V. A., 2003, *ApJ*, 590, 333
 Sutton E. C., Sobolev A. M., Saliu S. V., Malyshev A. V., Ostrovskii A. B., Zinchenko I. I., 2004, *ApJ*, 609, 231
 Tatematsu K., Umemoto T., Kameya O., Hirano N., Hasegawa T., Hayashi M., Iwata T., Kaifu N., Mikami H., Murata Y., Nakano M., Nakano T., Ohashi N., Sunada K., Takaba H., Yamamoto S., 1993, *ApJ*, 404, 643
 Val'tts I. E., Ellingsen S. P., Slysh V. I., Kalenskii S. V., Otrupcek R., Larionov G. M., 2000, *MNRAS*, 317, 315
 Voronkov M. A., Sobolev A. M., Ellingsen S. P., Ostrovskii A. B., Alakoz A. V., 2005, *ApSS*, 295, 217 (astro-ph/0407275)
 Whitworth A. P., Clarke C. J., 1997, *MNRAS*, 291, 578
 Wright M. C. H., Plambeck R. L., Wilner D. J., 1996, *ApJ*, 469, 216
 Zapata L. A., Rodríguez L. F., Kurtz S. E., O'Dell C. R., Ho P. T. P., 2004, *ApJ*, 610, L121
 Ziurys L. M., Wilson T. L., Mauersberger R., 1990, *ApJ*, 356, L25

This paper has been typeset from a $\text{\TeX}/\text{\LaTeX}$ file prepared by the author.